Available online at www.sciencedirect.com
ScienceDirect
Trans. Nonferrous Met. Soc. China 34(2024) 560−575
Transactions of Nonferrous Metals Society of China
www.tnmsc.cn

Numerical simulation of microstructure evolution in molten pool of nickel-based superalloy during selective laser melting

Yi QIU[1], Ying-ju LI[2], Xiao-hui FENG[2], Ang ZHANG[3], Yuan-sheng YANG[2]

1. School of Materials Science and Engineering, Beijing Institute of Technology, Beijing 100081, China;
2. Institute of Metal Research, Chinese Academy of Sciences, Shenyang 110016, China;
3. Collage of Materials Science and Engineering, Chongqing University, Chongqing 400044, China

Received 13 August 2022; accepted 5 May 2023

Abstract: The competitive growth and the evolution of grain/dendrite structures of IN718 superalloy in the molten pool during selective laser melting (SLM) were investigated with the finite element method (FEM) coupling the phase-field model (PFM). The thermal evolution was solved by the FEM and then the results were input into the PFM model to simulate the microstructure evolution involving grain nucleation, grain epitaxial growth and grain competition. Based on the analysis of microstructure evolution of the transverse and longitudinal sections of the molten pool, the mechanism of dendrite competitive growth in the SLM process was discussed and the concentration distribution of the solute element Nb in the molten pool was quantitatively calculated. The results show that the dendrite competitive growth is affected by both the temperature gradient and the crystallographic orientation. The unfavorable orientation grain with a high misorientation (>22.5°) will be eliminated by the favorable orientation grain quickly.

Key words: Ni-based superalloys; selective laser melting; phase-field model; grain/dendrite structures evolution; competitive growth

1 Introduction

In recent years, additive manufacturing (AM) has enabled the fabrication of single crystal parts, referred to as the new directional solidification [1,2]. The competitive growth between dendrites with different orientations becomes a key factor influencing the final microstructures and mechanical properties of the directional solidification [3]. However, the competitive growth of dendrites is complicated in the melt pool during AM process, and there is a lack of research on competitive growth [4,5]. Due to the high solidification rate during the SLM process, it is difficult to achieve microstructure evolution in-situ observation [6−8]. With the development of numerical simulation in recent years, microstructure evolution can be studied by numerical simulation and the phase-field model (PFM) has been used to simulate AM process [9,10].

Much attention has been paid to the simulation of the microstructure evolution in the molten pools at the dendrite scale and the grain scale. LIU and WANG [11] studied the effect of the latent heat of solidification on dendrite growth and their results show that the latent heat should be considered for simulating the dendrite growth. YU et al [12] demonstrated that the higher the anisotropy strength, the shorter the interface instability time. Some scholars carried out the calculation of multiple molten pools by the phase-field model (PFM) simulation at the grain scale. YANG et al [13] showed that the coarsening of grains in the remelting region was caused by epitaxial growth. LIU et al [14] indicated that the CET is critically

Corresponding author: Yuan-sheng YANG, Tel: +86-24-23971728, E-mail: ysyang@imr.ac.cn
DOI: 10.1016/S1003-6326(23)66417-9

controlled by undercooling, involving constitutional supercooling, thermal undercooling, and curvature undercooling in the molten pool. Their results showed that parts are generally composed of equiaxed, mixed grains and columnar grains [15]. The results show that the direction of grain growth is attributed to the cooperation and competition between the temperature gradient and the preferred crystal orientation. The heat flow makes the crystal grains bend to the temperature gradient direction. CHADWICK and VOORHEES [16] demonstrated that the grains bend in the scanning direction and got the same results as LIU et al did [14].

The above researches prove that the coupling FEM and PFM is an effective method to simulate the microstructure evolution of AM from different perspectives. However, the research on the competitive growth of dendrites is insufficient. It is worth noting that the secondary branches of the dendrites obtained by SLM would not be well developed due to the high temperature gradient and cooling rate. The research also shows that the secondary branch has a direct effect on the formation of grain boundaries and dendrite competition [17,18], but the mechanism of dendrite competitive growth in SLM is not clear.

The aim of this work is to reveal the competitive growth mechanisms in the melt pool to facilitate directional solidification by SLM. In this work, a multiscale framework combing the FEM and PFM on the scale of both grain and dendrite is employed to investigate microstructure evolution in the molten pool. A new model that is different from the previous model is developed in the present study, and the highlight is that the temperature field which is input in the PFM is updated by cubic spline interpolation in time and cubic convolution interpolation in space. Cubic convolution interpolation has second-order accuracy in space, which is higher than linear interpolation accuracy. The comparison of spatial interpolation was conducted in Section 2. Then, a widely used Ni-based superalloy IN718 is selected as the object of calculation in this study. The temperature field information obtained by FEM is used as the input of the PFM. Furthermore, the grain nucleation, grain epitaxial growth, and grain competition are included in the model. The predicted patterns of grain/dendrite are compared with experimental observations, and the mechanism of dendrite competitive growth in SLM is also investigated through the proposed approach.

2 Numerical simulation

2.1 Macro-scale thermal model

A FEM in which the mechanism of heat transfer was considered as heat conduction following the Fourier law was used to calculate the temperature field of the SLM process. The governing equation describing the temperature field is given as Eq. (1):

$$\rho C_p \frac{\partial T}{\partial t} = \frac{\partial}{\partial x}\left(\kappa \frac{\partial T}{\partial x}\right) + \frac{\partial}{\partial y}\left(\kappa \frac{\partial T}{\partial y}\right) + \frac{\partial}{\partial z}\left(\kappa \frac{\partial T}{\partial z}\right) + q(r) \tag{1}$$

where ρ, C_p and κ are the density, specific heat capacity and thermal conductivity, respectively. The last term on the right is the heat source which is expressed as a surface Gaussian heat source by Eq. (2):

$$q(r) = \frac{3Q}{\pi r_{\mathrm{a}}^2} \exp\left(-3\frac{r^2}{r_{\mathrm{a}}^2}\right) \tag{2}$$

where $3Q/(\pi r_{\mathrm{a}}^2)$ is thermal flux, r is the distance away from the center of the heat source, and r_{a} is the effective heat radius.

2.2 Micro-scale numerical method

2.2.1 Nucleation model

The continuous nucleation model proposed by THÉVOZ et al [19] was used to describe the heterogeneous nucleation process. The relation between the increase of nucleation density dn and the increase of undercooling ΔT follows a Gaussian distribution given as Eq. (3):

$$\frac{\mathrm{d}n}{\mathrm{d}(\Delta T)} = \frac{n_{\max}}{\sqrt{2\pi}(\Delta T_\sigma)} \exp\left[-\frac{1}{2}\left(\frac{\Delta T - \Delta T_{\mathrm{N}}}{\Delta T_\sigma}\right)^2\right] \tag{3}$$

where ΔT is the undercooling, ΔT_{N} is the average nucleation undercooling, ΔT_σ is the standard deviation, and $n_{\max}$ is the maximum nucleation. The nucleation density $n(\Delta T)$ at any undercooling can be calculated by

$$n(\Delta T) = \int_0^{\Delta T} \frac{\mathrm{d}n}{\mathrm{d}(\Delta T)} \mathrm{d}(\Delta T) \tag{4}$$

As the solidification proceeds, the temperature in the molten pool is reduced by δT within a time step, and the undercooling is reduced by $\delta(\Delta T)$. According to Eq. (4), the density of the newly formed crystal nuclei in this time step is

$$\delta n = n\left[\Delta T + \delta(\Delta T)\right] - n(\Delta T) = \int_0^{\Delta T+\delta(\Delta T)} \frac{\mathrm{d}n}{\mathrm{d}(\Delta T)}\mathrm{d}(\Delta T) - \int_0^{\Delta T} \frac{\mathrm{d}n}{\mathrm{d}(\Delta T)}\mathrm{d}(\Delta T) \quad (5)$$

At any time step, the point in the liquid phase is assigned a random number as the density of nucleation. If the density of nucleation of a point is smaller than δn and its undercooling exceeds ΔT_{N}, this point is assigned the solid phase.

2.2.2 Phase-field model

A 2D-PFM of binary alloy solidification with coupled heat and solute diffusion [20] was used in this work. In the PFM formulation, an order parameter ϕ is introduced to describe the phase at the given location and time. Specifically, ϕ=1 is regarded as the solid phase and ϕ=−1 is regarded as the liquid phase. Both the space and time are nondimensionalized ($\tilde{t}=t/\tau_0$, $\tilde{x}=x/W_0$) by interface width (W_0) and relaxation time (τ_0). The interface width is calculated by $W_0=\lambda d_0/a_1$ and the relaxation time τ_0 is expressed by

$$\tau_0 = (d_0^2/D)a_2\lambda^3/a_1^2 \quad (6)$$

where λ is the coupling coefficient, a_1=0.8839 and a_2=0.6267 are constants, $d_0=\Gamma/(T_{\mathrm{l}}-T_{\mathrm{s}})$ is the chemical capillary length, Γ is the Gibbs-Thomson coefficient, T_{l} and T_{s} are liquidus and solidus temperatures, respectively, and D is the liquid diffusion coefficient and diffusion in the solid phase is ignored. Then, the dimensionless governing equations are obtained as

$$a_{\mathrm{s}}(\vec{n})^2\left[\frac{1}{Le}+k(1+(1-k)U)\right]\partial_t\phi = \nabla\cdot\left[a_{\mathrm{s}}(\vec{n})^2\nabla\phi\right] + \partial_x\left[|\nabla\phi|^2 a_{\mathrm{s}}(\vec{n})\frac{\partial a_{\mathrm{s}}(\vec{n})}{\partial(\partial_x\phi)}\right] + \partial_y\left[|\nabla\phi|^2 a_{\mathrm{s}}(\vec{n})\frac{\partial a_{\mathrm{s}}(\vec{n})}{\partial(\partial_y\phi)}\right] - f'(\phi) - \lambda g'(\phi)(kU+T_\theta) \quad (7)$$

$$\frac{1+k-(1-k)\phi}{2}\partial_t U = \nabla\cdot\left\{\tilde{D}\frac{1+\phi}{2}\nabla U - \underbrace{a(\phi)\left[1+(1-k)U\right]\partial_t\phi\cdot\nabla\phi/|\nabla\phi|}_{j_{\mathrm{at}}}\right\} + \frac{1}{2}[1+(1-k)U]\partial_t\phi \quad (8)$$

where Le is Lewis number, k is the partition coefficient, $f'(\phi)=\phi^3-\phi$ and $g'(\phi)=(1-\phi^2)^2$ are the derivative of double-well potential function and the interpolation function, respectively, and T_θ is the nondimensional undercooling given by

$$T_\theta = \frac{T-T_{\mathrm{l}}}{T_{\mathrm{l}}-T_{\mathrm{s}}} = \frac{T-T_{\mathrm{l}}}{-m(1-k)c_{\mathrm{l}}^{\mathrm{e}}} \quad (9)$$

where T is temperature at each point, m is the liquidus slope, and $c_{\mathrm{l}}^{\mathrm{e}}$ is the equilibrium concentration.

The nondimensional supersaturation field U used to characterize the solute field is given by

$$U = \left(\frac{2c/c_{\mathrm{l}}^{\mathrm{e}}}{1+k-(1-k)\phi}-1\right)\cdot\frac{1}{1-k} \quad (10)$$

To eliminate the effects of interface stretching and surface diffusion, the anti-trapping current j_{at} proposed by KARMA [21] is coupled. $\tilde{D}=D\tau_0/W_0^2$ is the nondimensional diffusion coefficient according to nondimensionalized rule.

In addition, the anisotropy of the crystal also needs to be considered. $a_{\mathrm{s}}(\vec{n})$ is an anisotropy function in Eq. (7). The expression of $a_{\mathrm{s}}(\vec{n})$ is given by

$$a_{\mathrm{s}}(\vec{n}) = 1+\varepsilon_4\cos[4(\theta_0+\theta)] \quad (11)$$

where ε_4 is the strength of the anisotropy, θ_0 is the angle between the normal to the solid/liquid interface and the axis x, and θ is the rotation angle of the local coordinate system or the grain growth orientation [17]. The range of α is 0−π/2. For the liquid phase, the orientation is set to be 0. The number "4" in Eq. (11) represents the fourfold anisotropy in the 2-D system. The threshold $\beta_{i,j}$=0.01 is introduced to update the grain orientation information. If $-1.0\le\phi_{i,j}\le\beta_{i,j}$, $\theta_{i,j}$ is updated from its nearest neighbor point.

2.2.3 Polycrystalline solidification

In SLM process of the polycrystalline mental, the initial polycrystalline substrate and the orientation of grains need to be considered to simulate the solidification. There are two ways to describe polycrystals by the PFM. One is the

multi-phase model in which each order parameter represents a grain, and each grain has orientation information. The other is the orientation field model, which is built with orientation dynamics to simulate the evolution of the orientation field. We refer to the literature [22] on the treatment of the orientation field. In the current work that focus on the grain/dendrite microstructure evolution, it is unnecessary to consider the orientation dynamics because the grain/dendrite microstructure evolution is unaffected by the dynamics of the physical triple junction between the two grains and the liquid [18]. In addition, the initial polycrystalline substrate is obtained by solving Eqs. (7) and (8) at a fixed temperature. Equiaxed grains are randomly generated with a random orientation of 0−π/2.

2.3 Calculation parameters and temperature interpolation

The macro-scale heat transfer model was solved by the commercial finite element software ANSYS. The domain size of the FEM was 500 μm × 200 μm × 130 μm. The mesh size was 10 μm at the substrate zone and 3.3 μm at the additive part zone. Thermo-physical properties of alloy IN718 from references [14,23,24], as listed in Table 1, were used for the calculation. Singletrack simulation was run at given laser power (P: 150 W) and scanning speed (v: 500 mm/s). The temperature field was extracted from the FEM simulation and input into the PFM as illustrated in Fig. 1. Both the longitudinal section and the transverse section were selected to conduct the PFM simulation.

Table 1 Parameters and properties for simulations

Physical property	Value	Ref.
Liquid temperature, T_{liq}/°C	1404	[23]
Solid temperature, T_{sol}/°C	1369	[23]
Liquidus slope, m/(K·wt.%)	−10.5	[23,24]
Far-field concentration, c_∞/wt.%	5.08	
Liquid diffusion coefficient, D/(m^2·s^{-1})	3×10^{-9}	[23,24]
Gibbs-Thomson coefficient, Γ/(K·m)	3.65×10^{-7}	[23,24]
Partition coefficient, k	0.48	[23,24]
Chemical capillary length, d_0/m	6.4×10^{-9}	[24]
Average nucleation undercooling, ΔT_N/K	33.6	[14]
Standard deviation, ΔT_σ/K	5.0	[14]
Maximum nucleation, n_{max}/m^{-3}	1.0×10^9	
Anisotropy of surface tension, ε_4	0.1	
Interface width, W_0/m	1.875×10^{-9}	
Grid size, dx/m	1.5×10^{-9}	
Relaxation time, τ_0/s	1.936×10^{-7}	
Time step, dt/s	3.872×10^{-9}	

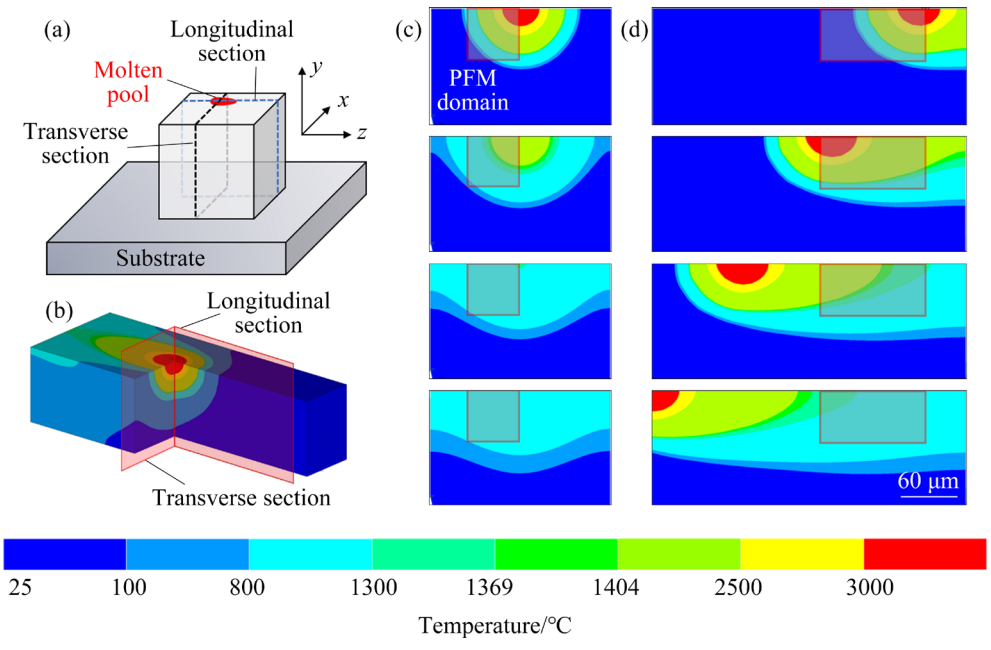

Fig. 1 Coupling procedure of thermal model with PFM: (a) Schematic diagram of transverse section and longitudinal section of molten pool; (b) Single track temperature field calculated by FEM; (c, d) Location of PFM calculation domain in FEM

A 2D domain with dimensions of 60 μm × 60 μm is used on transverse section. The longitudinal section domain size is 60 μm × 120 μm. The columnar grain growth is constrained by crystal growth and the main feature of constrained crystal growth is that the thermal flux direction is opposite to the growth direction. As shown in Fig. 2, the heat flows outwards from the molten pool center to the molten pool boundary. In particular, the heat flow directions are almost on the transverse plane (x−y plane) and perpendicular to the molten pool boundary. The heat flow propagating along the z direction is two orders of magnitude smaller than transverse plane. Thus, the heat flow can be considered as 2D in this work.

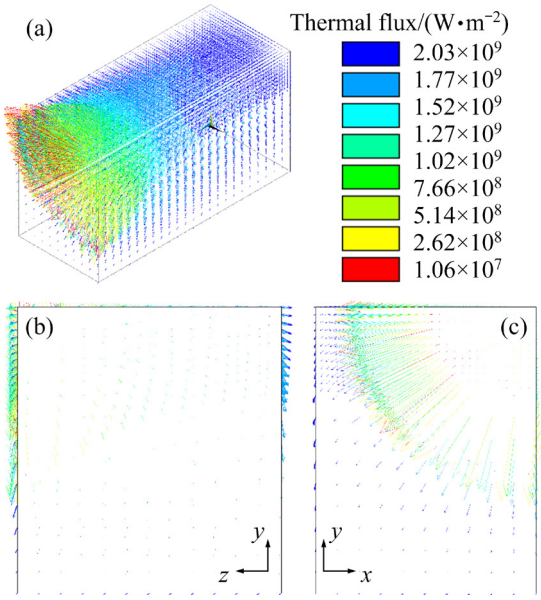

Fig. 2 Thermal information of SLM process: (a) Thermal flux distribution; (b) Thermal flux distribution on y−z plane; (c) Thermal flux distribution on x−y plane

Since the main alloying element is Nb in the IN718 superalloy and the second phase mainly consist of Ni and Nb, as an approximation, a Ni−Nb binary alloy was used for the PFM simulation [25,26]. The coupling coefficient was calculated by the interface width W_0 and chemical capillary length d_0 according to that $\lambda=a_1W_0/d_0$. The coupling coefficient was considered that it only changes with the interface width because the chemical capillary length is a constant for the material parameters. The quantitative phase-field model proposed by KARMA [21] was used to study the AM process when the interface width is in the order of capillary length [27]. Thus, W_0= 1.875×10^{-9} m was adopted to match the chemical capillary length, and the grid size in the PFM was $\mathrm{d}x=0.8W_0$, corresponding to 1.5×10^{-9} m. The Neumann boundary conditions with zero-flux were used for both phase and supersaturation fields. Time discretization adopted the forward Euler method and the time step needed to satisfy $\mathrm{d}t\leq(\mathrm{d}x)2/(4D)=1.875\times10^{-8}$ s. According Eq. (6), $\tau_0=1.936\times10^{-7}$ s, and $\mathrm{d}t=0.02\tau_0=3.872\times10^{-9}$ s was set to satisfy the convergence condition.

The FEM simulations were performed on a computer with Intel(R) Core(TM) i7-8550U CPU @1.80GHz and taken 1 h for FEM simulations. The PFM simulation was run on a platform with Xeon Gold-6230 @3.90GHz. Parallel computation with 80 threads was employed to accelerate the PFM simulation using the message passing interface (MPI). The computational time is about 20 h for PFM simulation.

The cubic spline interpolation was used to calculate the temperature within the FEM time step, and the interpolation was coupled the FEM and PFM in the time dimension. In this way, the inconsistency of the time and space steps between the FEM and the PFM was solved. Figure 3 shows the temperature information at the center point of the molten pool on the transverse section. The temperature reaches a peak at 0.0005 s and then the cooling process begins after this time.

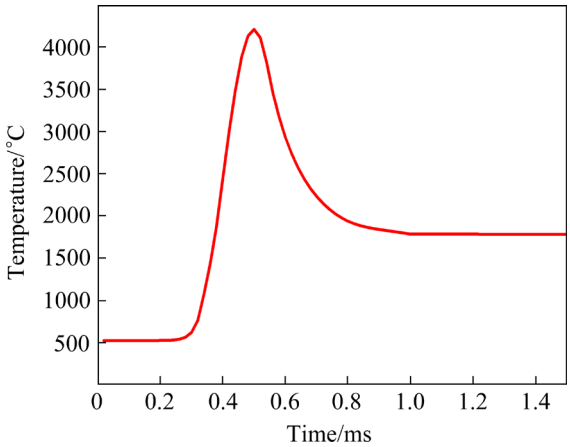

Fig. 3 Thermal circulation curve of center point of molten pool

The temperature field information was calculated by cubic convolution interpolation for the FEM grid size of 3.3 μm and the PFM grid size of 0.015 μm. The temperature at each point of the PFM calculation domain was calculated by

$$F(i+v,j+u)=\boldsymbol{A}\cdot\boldsymbol{B}\cdot\boldsymbol{C} \tag{12}$$

$$\boldsymbol{A}=(S(1+v)\quad S(v)\quad S(1-v)\quad S(2-v)) \tag{13}$$

$$\boldsymbol{B}=\begin{pmatrix} f(i-1,j-1) & f(i-1,j) & f(i-1,j+1) & f(i-1,j+2) \\ f(i,j-1) & f(i,j) & f(i,j+1) & f(i,j+2) \\ f(i+1,j-1) & f(i+1,j) & f(i+1,j+1) & f(i+1,j+2) \\ f(i+2,j-1) & f(i+2,j) & f(i+2,j+1) & f(i+2,j+2) \end{pmatrix} \tag{14}$$

$$\boldsymbol{C}^{\mathrm{T}}=\begin{pmatrix} S(1+u) & S(u) & S(1-u) & S(2-u) \end{pmatrix} \tag{15}$$

$$S(x)=\begin{cases} 1-(2.5)x^2+(1.5)|x|^3, & 0\leqslant|x|\leqslant 1 \\ 2-4|x|+2.5x^2-0.5|x|^3, & 1<|x|\leqslant 2 \end{cases} \tag{16}$$

where the subscripts i and j mean the nodal point in FEM, the subscript v represents the deviation of the number of rows, u represents the deviation of the number of columns in the PFM, and $S(x)$ is the convolution kernel.

Figure 4 shows the comparison of two spatial interpolation methods for the temperature field calculation results to the FEM temperature field. It can be seen that the temperature field calculated by the cubic convolution interpolation agrees with the FEM results. Compared with the temperature field calculated by the bilinear interpolation, the temperature field calculated by the cubic convolution interpolation is smooth.

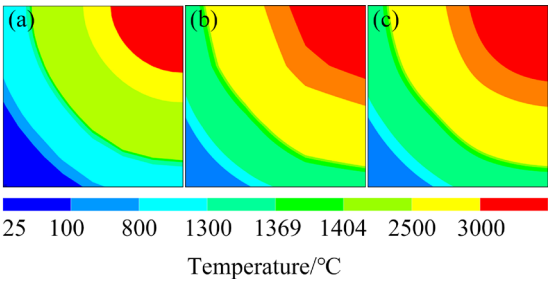

Fig. 4 Comparison of temperature field results: (a) FEM; (b) Bilinear interpolation; (c) Cubic convolution interpolation

3 Experimental details

SLM experiments were performed to verify the multiscale framework. A commercial In718 alloy for our experiments, with powder diameters ranging from 25 to 50 μm. The laser power and scanning speed were used with the same parameters as the finite element, i.e., a laser power of 150 W and a scanning speed of 500 mm/s. The actual experiment was not a single-pass experiment. A 10 mm × 10 mm × 10 mm block sample was built using an SLM system (EOS M290). The scanning strategy used bidirectional scanning with 66.7° rotation between layers. The laser spot diameter was 100 μm and the hatch distance was 50 μm. The layer thickness was 30 μm. The as-built sample was mounted, and fine-polished. The microstructure images were obtained using electron channeling contrast imaging (ECCI).

4 Results and discussion

4.1 Comparison of experimental and simulation results

To guarantee the accuracy of the simulated results, the simulated results were validated by comparison with the experimental results. Figure 5 shows simulated grain morphology and ECCI image of the IN718 alloy of an SLM sample. In Fig. 5(a), the columnar grains that grow near the fusion line have the same orientation as the substrate grain. The columnar grains with the different grain orientations in the bottom of molten pool can be observed in Figs. 5(b) and (c). In addition, Figs. 5(b) and (c) clearly show that the columnar grains consist of a group of columnar dendrites with the same growth direction. In Fig. 5(b), the grain marked by the yellow line exists in two molten pools, while the grain marked by the green line of the surrounding grains exists independently in one molten pool. The growth direction of the columnar grain is affected by both temperature gradient and crystallographic orientation. In Fig. 5(d), the temperature gradient direction is perpendicular to the molten pool boundary. As shown in Fig. 5(c), the white arrows are the direction of the temperature gradient and the black arrows are the growth direction of the columnar dendrites. In Fig. 5(c), it can be seen that there is an angle between the growth direction of the columnar dendrites and the direction of the temperature gradient, due to the growth direction of the columnar dendrite depending on the crystallographic orientation. The columnar grain orientation is similar to the grain orientation of the previous layer. At the bottom-left corner of the molten pool shown in Fig. 5(b), the growth direction of the columnar grain is perpendicular to the growth direction of the columnar grain in the previous track, which may be attributed to the four

preferred growth directions with an included angle of 90° for the cubic system, and the temperature gradient direction of the previous track is different from the latter scanning track.

Figure 6 shows the simulated dendrite microstructure and the ECCI image of IN718 superalloy microstructure. The primary dendrite arm space (PDAS) was measured from the concentration results. Figure 6 shows the comparison of PDAS between the simulated and the experimental results. The simulated PDAS ranges from 0.5 to 0.7 μm, which agrees well with the experiment results varying between 0.5 and 0.67 μm, validating the accuracy of the numerical simulation.

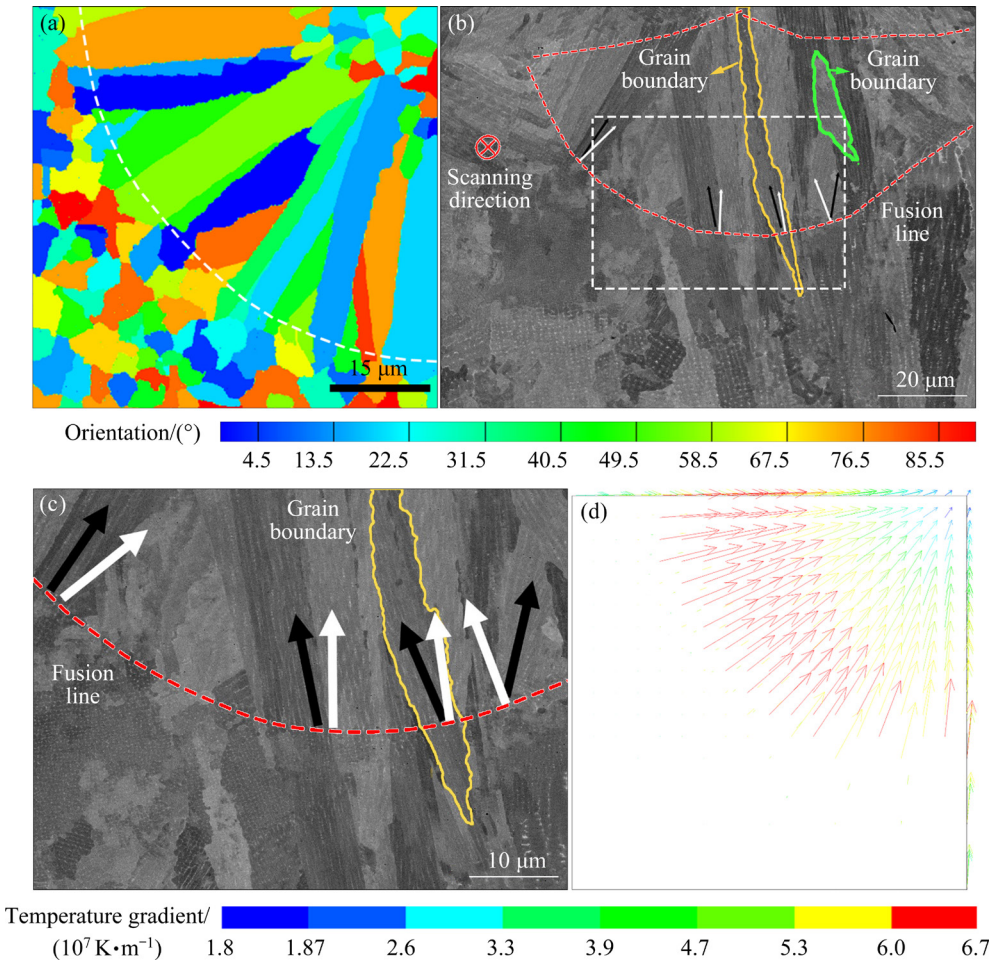

Fig. 5 Comparison of experimental and simulation results of microstructure of IN718 alloy manufactured by SLM: (a) Simulation result of grain morphology; (b) ECCI image of solidified microstructure in molten pool; (c) Magnification image of white dashed box in (b); (d) Temperature gradient obtained by FEM

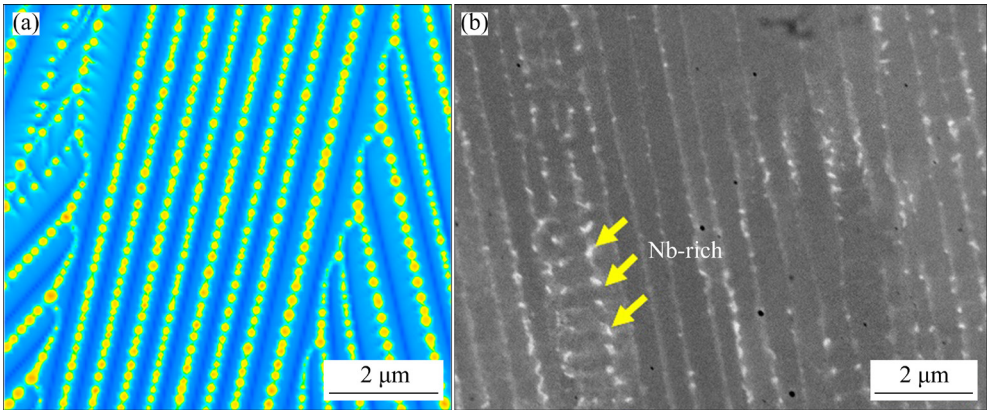

Fig. 6 Microstructures of simulated (a) and ECCI (b) IN718 alloy

Besides, there is a Nb concentration at the inter-dendritic space as shown in Fig. 6, which can cause the formation of the eutectic phases [28−30]. The columnar dendrites grow with the continuous formation of secondary branches. The closure of the secondary branches will block the diffusion of Nb in the liquid channel. The concentration of Nb atoms promote the formation of the Nb-rich eutectic phase.

4.2 Grain/dendrite evolution in molten pool

4.2.1 Transverse section

The grain/dendrite evolution simulated for a single track of SLM is shown in Fig. 7. In Fig. 7(a), the grains initially grow in planar morphology near the fusion boundary which can be verified from the thin layer of the planar grain (about 1 μm in thickness) in the magnification area. With the proceeding of solidification, the epitaxial growth dominates, and the solidification morphology changes from planar to columnar in the molten pool. Two categories of columnar grains can be found in Figs. 7(c) and (f). One category of columnar grains formed near the fusion line, and the other formed in the middle of the molten pool which is marked by the ellipse dotted line. The columnar grains near the fusion line have the same orientation as the substrate grains do. Besides, it is noticed that the undercooling at the front of the solid−liquid interface becomes larger with the process of solidification. As shown by the yellow arrows in Fig. 7(b), the undercooling drives the formation of new nuclei. Because the undercooling between two divergence columnar dendrites is larger than that between parallel columnar dendrites [31], the nucleation of the new grains will take place between the two divergence columnar dendrites. According to Eq. (3), a larger undercooling will increase the nucleation probability. In the middle of the molten pool, the thermal flux direction is from the centerline to the fusion line which is reversed to the growth direction. Grains with an aspect ratio a_r large than 2.55 are easily formed at this stage. Specifically, a_r>2.55 represents the columnar grains, 2.55>a_r>1.75 for the mixed grains, and a_r<1.75 for the equiaxed grains [15,32,33].

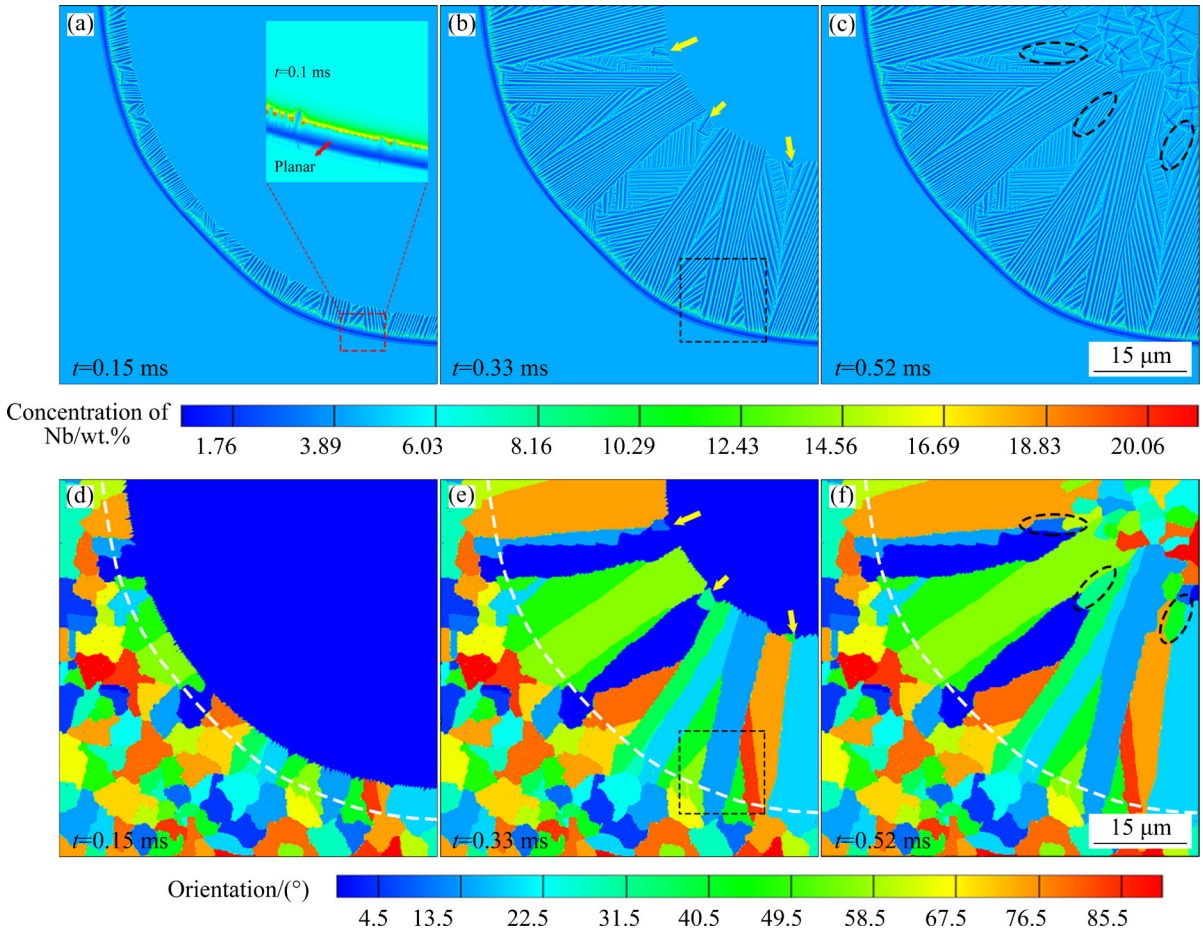

Fig. 7 Grain/dendrite microstructure evolution in molten pool: (a−c) Concentration field; (d−f) Orientation field

At the final stage of solidification, a large number of equiaxed grains formed ahead of the solidification front. With the temperature decreasing, both the temperature field and the thermal flux direction were changed, no longer from the fusion line to the centerline. The growth of the columnar grains was blocked by the equiaxed grains, which emerged in the last period. Then the equiaxed grains grow up till the solidification finish. This stage is also called CET (columnar to equiaxed grain transition) and is usually close to the last stage of solidification.

4.2.2 Longitudinal section

Figure 8 shows the microstructure evolution on the longitudinal section of the molten pool. Epitaxial growth occurs at the initial solidification stage with the transverse section. The direction of the temperature gradient on the longitudinal section changes as the heat source moves. As the heat source moves from right to left, the columnar grains at the bottom are deflected to the left. That is related to the change of the heat flow direction. In the beginning, the direction of the temperature gradient at the bottom of the molten pool is perpendicular to the fusion line. With continuous movement of the heat source, the direction of the temperature gradient deviates, and the growth direction is inclined toward the temperature gradient direction. The co-action of the crystal orientation and the temperature gradient results in the competitive growth.

The columnar grains at the bottom of the molten pool incline toward the scanning direction (SD) as shown in Fig. 9. The texture of ⟨001⟩//SD is formed at the upper of the molten pool and the texture of ⟨001⟩//BD (building direction) is formed at the bottom of the molten pool. As the undercooling at the solid−liquid interface increases, the nucleation density increases. More equiaxed grains will grow up which block the growth of columnar grains.

4.3 Competitive growth

The solidification process turns into competitive growth after epitaxial growth. The competitive growth of dendrites is controlled by the temperature gradient and solute diffusion at a low growth rate [34]. At the high cooling rate and the high growth rate, the competitive growth of the dendrites is mainly controlled by the temperature gradient because of the small diffusion region. In this case, the growth rate of the columnar grain with large misorientation is smaller than that of the grain with little misorientation. The columnar grain with

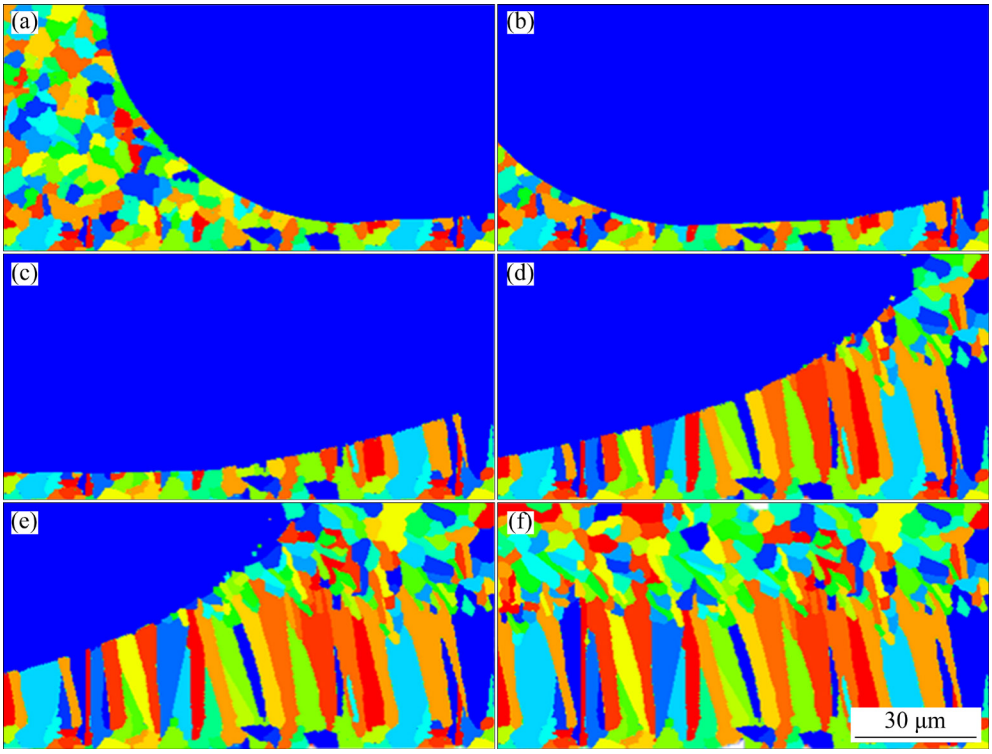

Fig. 8 Microstructure evolution on longitudinal section of molten pool: (a) *t*=0.07 ms; (b) *t*=0.15 ms; (c) *t*=0.23 ms; (d) *t*=0.38 ms; (e) *t*=0.46 ms; (f) *t*=0.62 ms

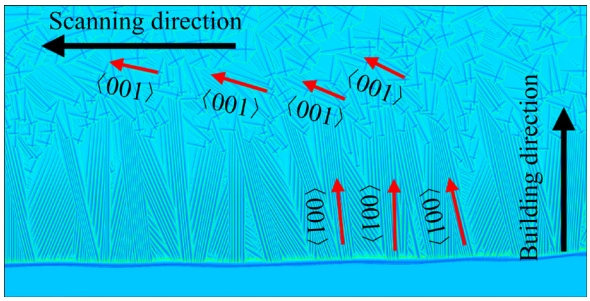

Fig. 9 Microstructure on longitudinal section of molten pool

a large growth rate will block the growth of other columnar grains. In low-speed laser processing, there are generally two competing growth mechanisms for columnar grains in the molten pool [22]. One is that the favorable orientation (FO) grains grow rapidly and form secondary branches and then the growth of the secondary branches prevents the growth of unfavorable oriented (UO) grains. The second is that when the UO grains encounter the grain boundaries of the FO grains, the growth of UO grains is inhibited due to less space for continued growth. In the SLM process the secondary branches cannot grow up, so the competitive growth mechanism is the second one described above. The grain boundaries formed by the FO grains make the UO grains weed out.

To quantitatively analyze the dendritic competitive growth, it is necessary to calculate the temperature gradient and the dendrite tip velocity. The direction of the temperature gradient was calculated according to Eq. (17), where $\theta_{G\text{-}y}$ is the angle between the direction of the temperature gradient and the y axis, and G_x and G_y are the components of the temperature gradient on the x and y axes, respectively. The dendrite tip velocity and the components of the dendrite tip velocity along the temperature gradient direction were calculated according to Eqs. (18) and (19), respectively, where (x_1, y_1) and (x_2, y_2) are the positions of the dendrite tip at different time. The dendrite tip position is in the range of (−1, 1). The point with ϕ=1 nearest to the interface was selected as the position for calculation. It can be seen from Figs. 10(c, d) that the difference between the real tip position and the calculated position is less than one grid. Since the interface width is constant, the error in calculating the tip velocity can be neglected.

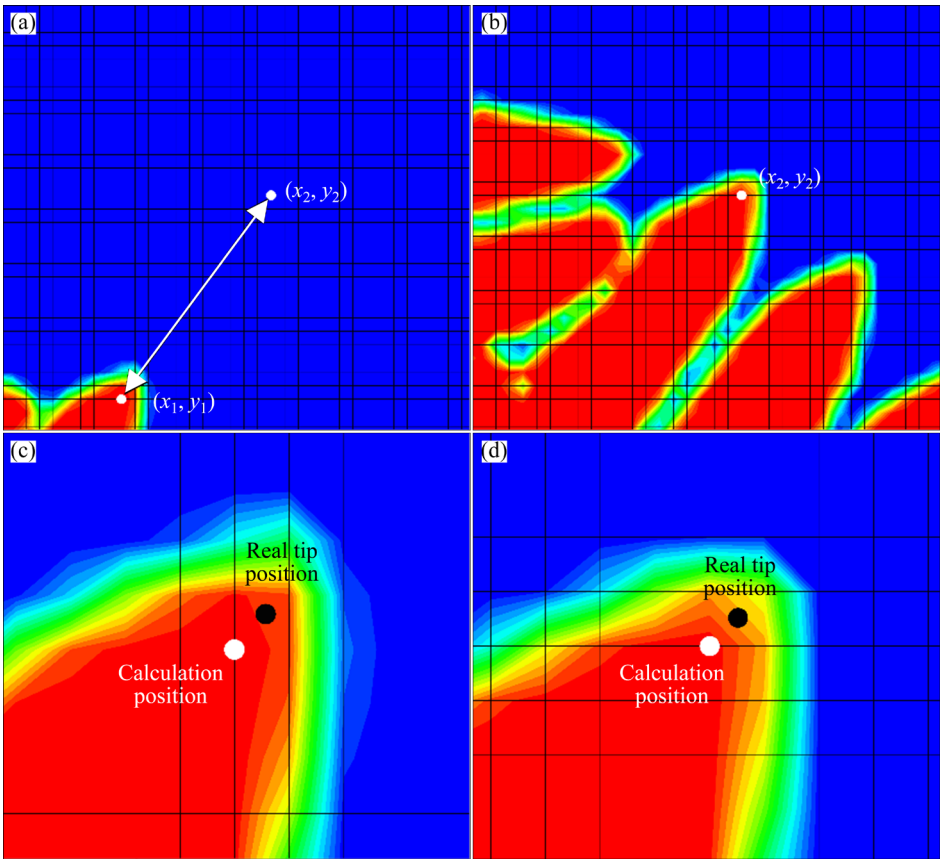

Fig. 10 Tip positions at different time: (a) At time t_1; (b) At time t_2; (c) Enlarged view of (a); (d) Enlarged view of (b)

$$\theta_{G\text{-}y} = \arctan\frac{G_x}{G_y} \tag{17}$$

$$v = \frac{\sqrt{(x_2 - x_1)^2 + (y_2 - y_1)^2}}{t_2 - t_1} \tag{18}$$

$$v_g = v \cdot \cos\left(\left|\theta - \theta_{G-y}\right|\right) \tag{19}$$

Figure 11 shows the competitive growth of two convergent grains at the initial stage of solidification. According to Eq. (16), $\theta_{G\text{-}y}$ is 19° at the grain boundary, then the misorientation of Grain A and Grain B are 36.0° and 5.5°, respectively. So the dendrite tip velocity of Grain A is 71 mm/s and Grain B is 122 mm/s, the v_g of Grain A is 57 mm/s and Grain B is 121 mm/s. As a result, Grain A will be eliminated by Grain B as shown in Figs. 11(c) and (d).

Figure 12 shows the competitive growth of dendrites at the middle stage of solidification during SLM. Different from that at the initial stage, the dendrite growth at this stage is accelerated. The growth information and misorientations of the two grains in Fig. 12 are given in Table 2. The competition between Grain A and Grain B at this stage is different from that at the initial stage because of the change of grain growth rate. The growth rate of Grain A and Grain B is constantly changing. The grain with a high growth rate will eliminate the grain with a low growth rate. Grain A and Grain B grow alternately near the grain boundary. It can be seen that the competition between the grains is changed in the case of small misorientation, and the dendrites near the grain boundary would be eliminated.

In addition to the converging grain boundaries, there are divergent grain boundaries in the molten pool during solidification of SLM. Figure 13 shows the competitive growth in the case of grain divergence. Unlike the converging grain boundary, the divergent grain boundary rarely results in the elimination of grains. Because there is the growth space nearby the grain boundary, the secondary branch and the tertiary branch will form and grow

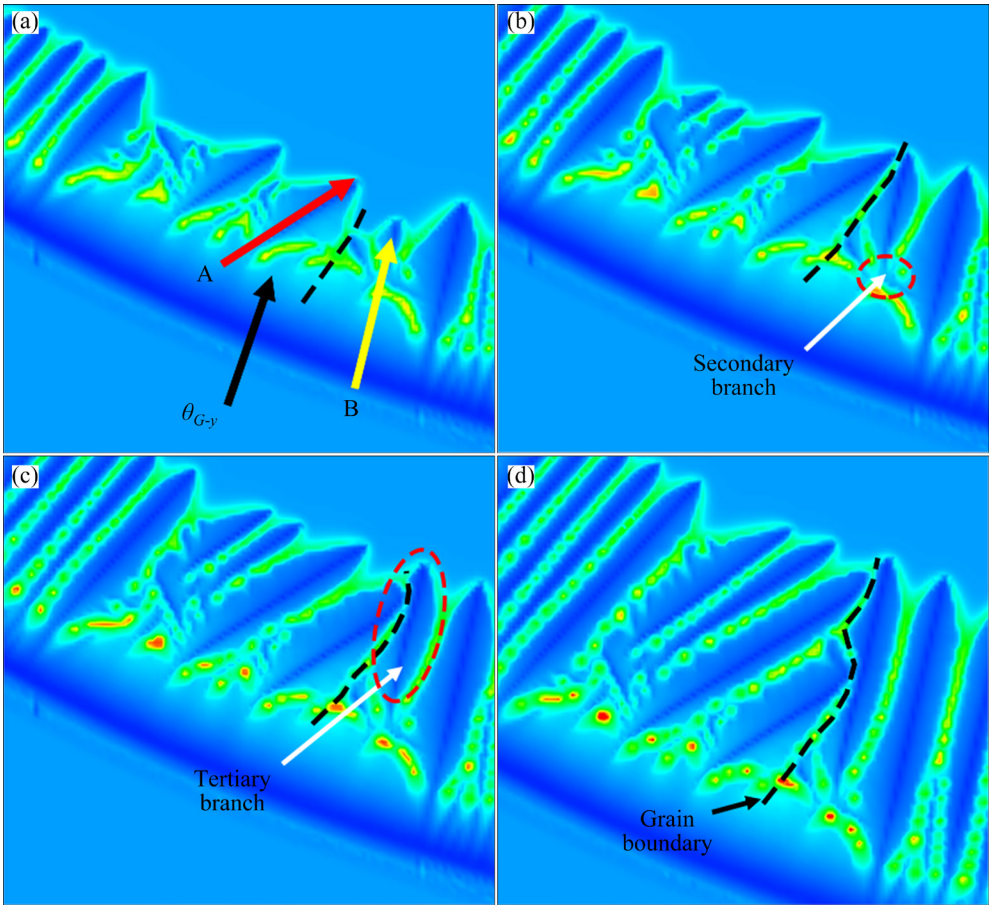

Fig. 11 Competitive growth of dendrites at initial stage of solidification: (a) Dendrite orientation and temperature gradient direction; (b) Secondary branch on side of primary dendrite; (c) Tertiary branch; (d) Grain boundary formed by competitive growth

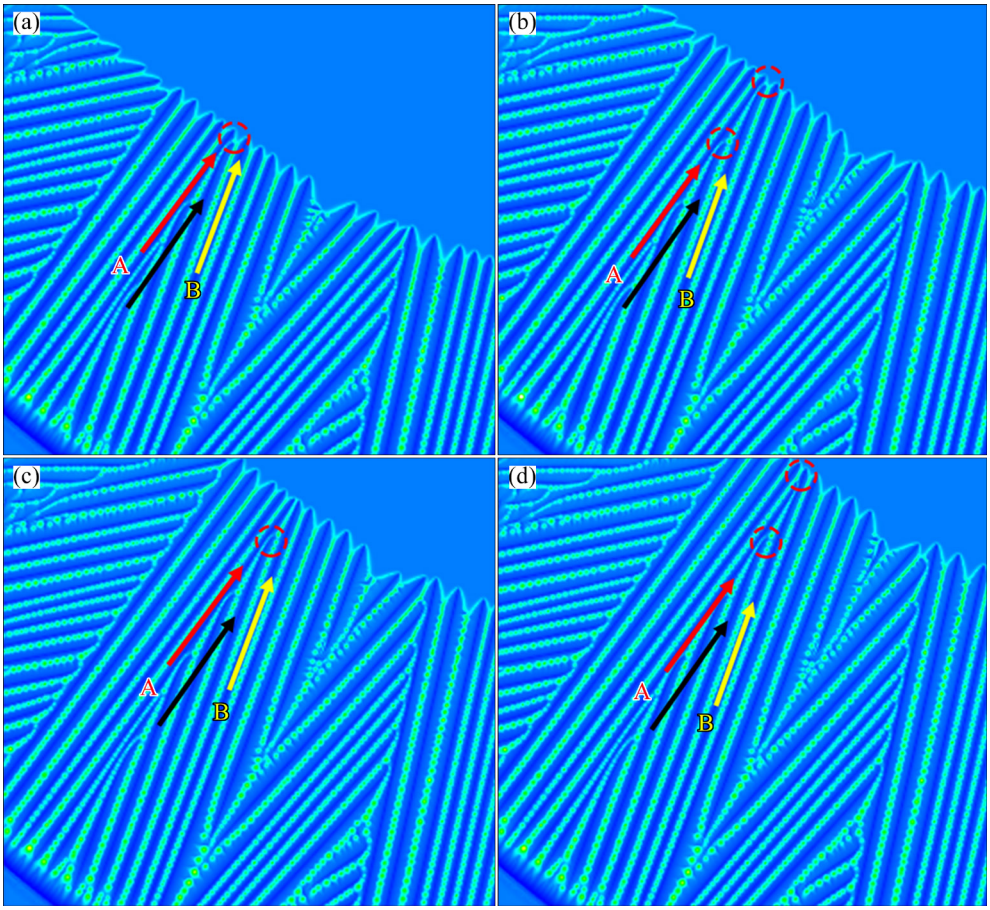

Fig. 12 Competitive growth of dendrites at middle of solidification: (a, b) Stage I; (c, d) Stage II

Table 2 Competitive growth information in Fig. 12

Stage	Grain	θ/(°)	$\lvert\theta-\theta_{G\text{-}y}\rvert$/(°)	v/(mm·s^{-1})	v_g/(mm·s^{-1})
I	A	36.9	2.05	140	139.9
	B	21.6	13.25	140	136.2
II	A	36.9	2.08	151	150.9
	B	21.6	13.22	158	153.8

up nearby the grain boundary. The formation of the secondary branches is also affected by the misorientation. The secondary branches easily form when the misorientation is larger. Based on the angle between the temperature gradient and the y axis which is 28.2°, the misorientations of the three grains in Fig. 14 can be calculated and they are 6.7°, 13.2°, and 27.6°, respectively. Therefore, the secondary branch would be formed when the columnar dendrite with a misorientation of 27.6°.

On the longitudinal section of the molten pool, the direction of the temperature gradient changes as the heat source moves. This change results in the misorientations being different at each time, so the competition between grains changes, as shown in Fig. 15. The specific competitive growth information is shown in Table 3. At stage I, the angle between the temperature gradient direction and the scanning direction is 72.8°. The misorientation of Grain A is smaller than that of Grain B. The v_g of Grain A is larger than that of Grain B. The columnar dendrite of Grain B at the grain boundary is eliminated, as shown by the red dotted coil in Fig. 15(b). At Stage II, the direction of the temperature gradient changes greatly, and the angle between the temperature gradient direction and the scanning direction is 61.0°. The misorientation of Grain A is larger than that of Grain B,

Table 3 Competitive growth information in Fig. 15

Stage	Grain	θ/(°)	$\theta_{G\text{-}y}$/(°)	$\lvert\theta-\theta_{G\text{-}y}\rvert$/(°)	v/(mm·s^{-1})	v_g/(mm·s^{-1})
I	A	81.9	72.8	9.1	134.3	132.6
	B	65.7		7.1	131.7	130.7
II	A	81.9	61	20.9	205.3	191.8
	B	65.7		4.7	204	203.3

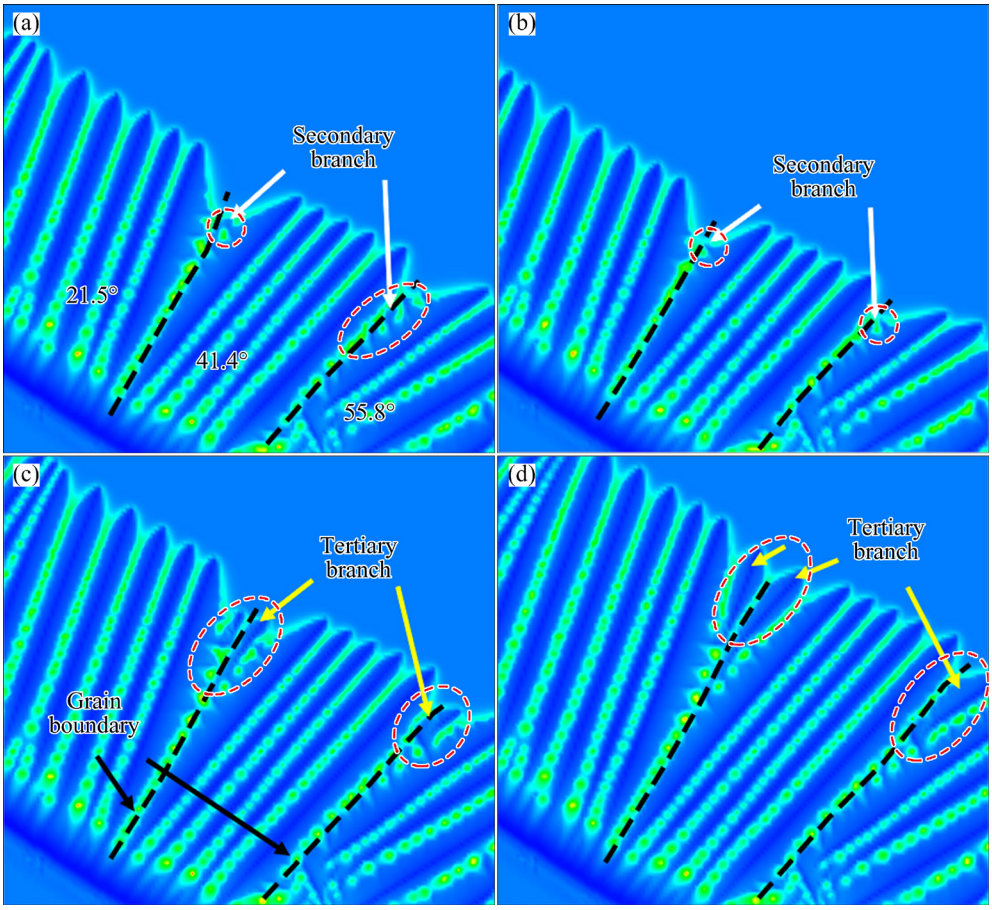

Fig. 13 Competitive growth of dendrites at divergent grain boundaries: (a) Misorientation angle of each grain; (b) Secondary branch at grain boundaries; (c−d) Tertiary branch at grain boundaries

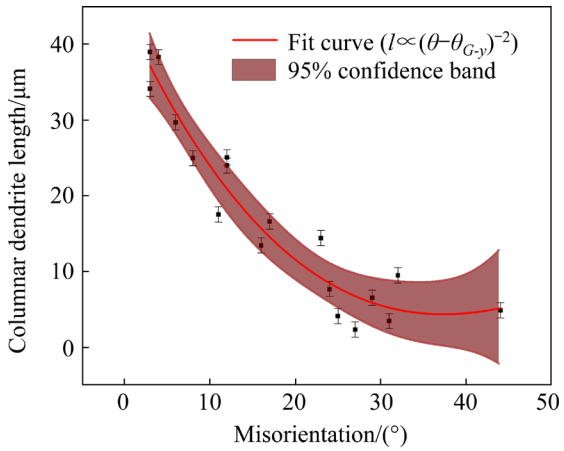

Fig.14 Relation between misorientation and columnar dendrite length

and the velocity component of Grain A is smaller than that of Grain B. Dendrites of Grain A are eliminated. Then, a large number of new nucleated grains form and block the growth of columnar dendrites.

The effect of the misorientation on the microstructure can be analyzed by the size of columnar grains. Because of the complex evolution of microstructure in the molten pool, the length of primary dendrite within a grain was measured instead of grain length. Figure 14 illustrates the relation between the misorientation ($|\theta-\theta_{G\text{-}y}|$) and the columnar dendrite length (l) on the transverse section. It shows that the columnar dendrite length and $(\theta-\theta_{G\text{-}y})^2$ are inversely proportional. When $|\theta-\theta_{G\text{-}y}|$ is greater than 22.5°, the columnar dendrite length remains unchanged. This means that the columnar dendrites with high misorientation ($|\theta-\theta_{G\text{-}y}|>22.5°$) are eliminated.

5 Conclusions

(1) The solidification structure of the SLM molten pool consists of the columnar grain region, the mixed grain region, and the equiaxed grain region. There are two sources of columnar dendrites in the molten pool of SLM, one is epitaxial growth of the substrate grains, and the other is formation of nucleation and growth under the action of heat flow.

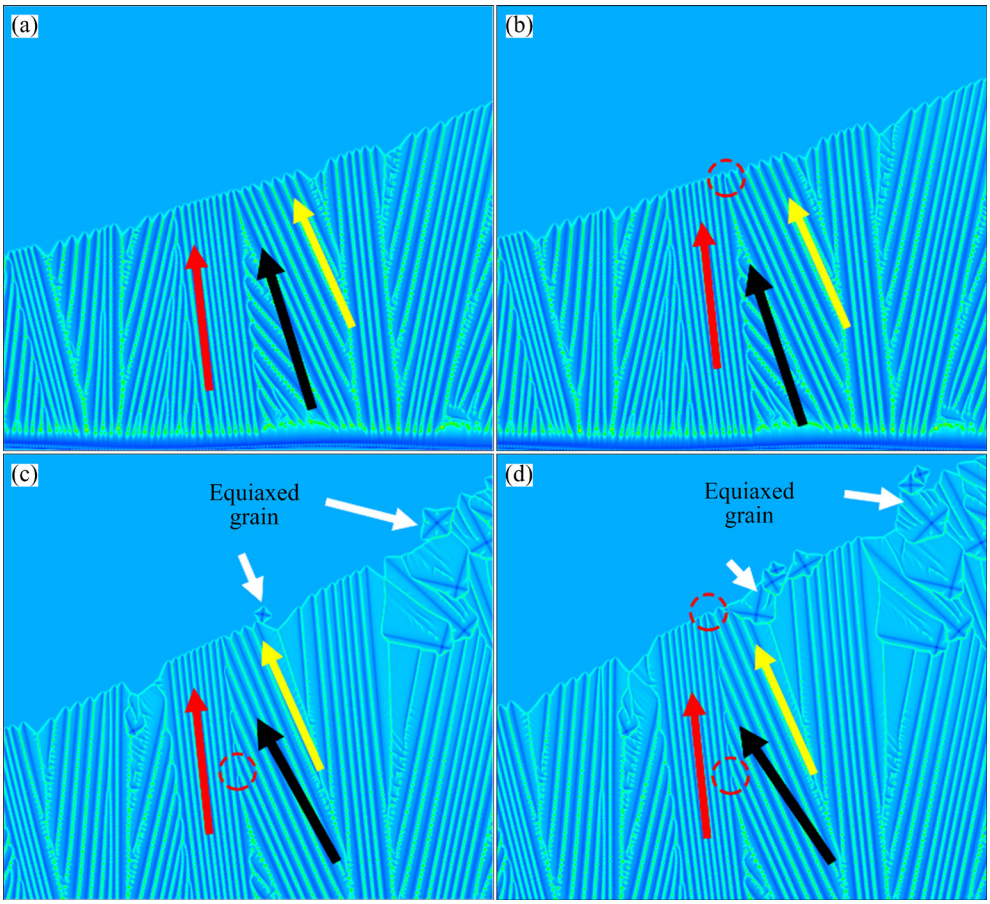

Fig. 15 Competitive growth of dendrites in longitudinal section: (a−b) Stage I; (c−d) Stage II

(2) The competition mechanism of dendrite growth in the melt pool is that the FO grains formed at grain boundaries eliminate the UO grains. The dendrite competitive growth is influenced by the misorientation. The grains with high misorientation ($|\theta-\theta_{G\text{-}y}|>22.5°$) will be eliminated on the transverse section of the molten pool.

(3) The change of direction of the temperature gradient due to the heat source moves on the longitudinal section of the molten pool results in the variation of the velocity component in the temperature gradient direction. The growth direction of the columnar grains at the bottom of the molten pool is deflected to the scanning direction on the longitudinal section of the molten pool.

CRediT authorship contribution statement

Yi QIU: Methodology, Software, Investigation, Analysis, Writing − Original Draft; **Ying-ju LI:** Funding Acquisition, Supervision; **Xiao-hui FENG:** Supervision, Writing − Review & Editing; **Ang ZHANG:** Writing − Review & Editing; **Yuan-sheng YANG:** Funding Acquisition, Writing − Review & Editing.

Declaration of competing interest

The authors declare that they have no known competing financial interests or personal relationships that could have appeared to influence the work reported in this paper.

Acknowledgments

This work was financially supported by the National Science and Technology Major Project, China (No. Y2019-VII-0011-0151). The authors thank Dr. Shao-ning GENG (Huazhong University of Science and Technology) and Dr. Cheng-chao DU (Jiangsu University) for their help.

References

[1] MURR L E, MARTINEZ E, GAYTAN S M, RAMIREZ D A. Contributions of light microscopy to contemporary materials characterization: the new directional solidification [J]. Metallography, Microstructure, and Analysis, 2012, 1(1): 45−58.

[2] LI Yang, LIANG Xiao-yu, YU Ye-feng, WANG Dong-fang, LIN Feng. Review on additive manufacturing of single-crystal nickel-based superalloys [J]. Chinese Journal of

Mechanical Engineering: Additive Manufacturing Frontiers, 2022, 1(1): 100019.

[3] GUO Chun-wen, LI Jun-jie, WANG Zhi-jun, WANG Jin-cheng. Non-uniplanar competitive growth of columnar dendritic grains during directional solidification in quasi-2D and 3D configurations [J]. Materials & Design, 2018, 151: 141−153.

[4] SITINUR H M R, LIM L X, LOCKMAN Z, ZUHAILAWATI H. Fabrication of titanium-based alloys with bioactive surface oxide layer as biomedical implants: Opportunity and challenges [J]. Transactions of Nonferrous Metals Society of China, 2022, 32(1): 1−44.

[5] YUE Tian-yang, ZHANG Sheng, WANG Chao-yue, XU Wei, XU Yi-di, SHI Yu-sheng, ZANG Yong. Effects of selective laser melting parameters on surface quality and densification behaviours of pure nickel [J]. Transactions of Nonferrous Metals Society of China, 2022, 32(8): 2634−2647.

[6] GUO Qi-lin, ZHAO Cang, QU Ming-lei, XIONG Liang-hua, HOJJATZADEH S M H, ESCANO L I, PARAB N D, FEZZAA K, SUN Tao, CHEN Lian-yi. In-situ full-field mapping of melt flow dynamics in laser metal additive manufacturing [J]. Additive Manufacturing, 2020, 31: 100939.

[7] HOJJATZADEH S M H, PARAB N D, YAN W, GUO Q, XIONG L, ZHAO C, QU M, ESCANO L I, XIAO X, FEZZAA K, EVERHART W, SUN T, CHEN L. Pore elimination mechanisms during 3D printing of metals [J]. Nat Commun, 2019, 10(1): 3088.

[8] ZHAO C, PARAB N D, LI X, FEZZAA K, TAN W, ROLLETT A D, SUN T. Critical instability at moving keyhole tip generates porosity in laser melting [J]. Science, 2020, 370(6520): 1080−1086.

[9] BAILEY N S, HONG K M, SHIN Y C. Comparative assessment of dendrite growth and microstructure predictions during laser welding of Al 6061 via 2D and 3D phase field models [J]. Computational Materials Science, 2020, 172: 109291.

[10] KARAYAGIZ K, JOHNSON L, SEEDE R, ATTARI V, ZHANG B, HUANG Xue-qin, GHOSH S, DUONG T, KARAMAN I, ELWANY A, ARRÓYAVE R. Finite interface dissipation phase field modeling of Ni−Nb under additive manufacturing conditions [J]. Acta Materialia, 2020, 185: 320−339.

[11] LIU De-hao, WANG Yan. Mesoscale multi-physics simulation of rapid solidification of Ti−6Al−4V alloy [J]. Additive Manufacturing, 2019, 25: 551−562.

[12] YU Feng-yi, WEI Yan-hong, LIU Xiang-bo. The evolution of polycrystalline solidification in the entire weld: A phase-field investigation [J]. International Journal of Heat and Mass Transfer, 2019, 142: 118450.

[13] YANG Min, WANG Lu, YAN Wen-tao. Phase-field modeling of grain evolutions in additive manufacturing from nucleation, growth, to coarsening [J]. NPJ Computational Materials, 2021, 7: 56.

[14] LIU Peng-wei, WANG Zhuo, XIAO Yao-hong, HORSTEMEYER M F, CUI Xiang-yang, CHEN Lei. Insight into the mechanisms of columnar to equiaxed grain transition during metallic additive manufacturing [J]. Additive Manufacturing, 2019, 26: 22−29.

[15] LIU P W, JI Y Z, WANG Z, QIU C L, ANTONYSAMY A A, CHEN L Q, CUI X Y, CHEN L. Investigation on evolution mechanisms of site-specific grain structures during metal additive manufacturing [J]. Journal of Materials Processing Technology, 2018, 257: 191−202.

[16] CHADWICK A F, VOORHEES P W. The development of grain structure during additive manufacturing [J]. Acta Materialia, 2021, 211: 116862.

[17] TOURRET D, SONG Y, CLARKE A J, KARMA A. Grain growth competition during thin-sample directional solidification of dendritic microstructures: A phase-field study [J]. Acta Materialia, 2017, 122: 220−235.

[18] TOURRET D, KARMA A. Growth competition of columnar dendritic grains: A phase-field study [J]. Acta Materialia, 2015, 82: 64−83.

[19] THÉVOZ P, DESBIOLLES J L, RAPPAZ M. Modeling of equiaxed microstructure formation in casting [J]. Metallurgical Transactions A, 1989, 20: 311−322.

[20] RAMIREZ J C, BECKERMANN C, KARMA A, DIEPERS H J. Phase-field modeling of binary alloy solidification with coupled heat and solute diffusion [J]. Physical Review E, 2004, 69: 051607.

[21] KARMA A. Phase-field formulation for quantitative modeling of alloy solidification [J]. Physical Review Letters, 2001, 87(11): 115701.

[22] GENG Shao-ning, JIANG Ping, GUO Ling-yu, GAO Xue-song, MI Gao-yang. Multi-scale simulation of grain/sub-grain structure evolution during solidification in laser welding of aluminum alloys [J]. International Journal of Heat and Mass Transfer, 2020, 149: 119252.

[23] NIE Pu-lin, OJO O A, LI Zhu-guo. Numerical modeling of microstructure evolution during laser additive manufacturing of a nickel-based superalloy [J]. Acta Materialia, 2014, 77: 85−95.

[24] XIAO Wen-jia, LI Si-meng, WANG Cun-shan, SHI Yan, MAZUMDER J, XING Hui, SONG Li-jun. Multi-scale simulation of dendrite growth for direct energy deposition of nickel-based superalloys [J]. Materials & Design, 2019, 164: 107553.

[25] KUNDIN J, MUSHONGERA L, EMMERICH H. Phase-field modeling of microstructure formation during rapid solidification in Inconel 718 superalloy [J]. Acta Materialia, 2015, 95: 343−356.

[26] DENG Dun-yong, PENG Ru-lin, SÖDERBERG H, MOVERARE J. On the formation of microstructural gradients in a nickel-base superalloy during electron beam melting [J]. Materials & Design, 2018, 160: 251−261.

[27] KAVOUSI S, NOVAK B R, MOLDOVAN D, ASLE ZAEEM M. Quantitative prediction of rapid solidification by integrated atomistic and phase-field modeling [J]. Acta Materialia, 2021, 211: 116885.

[28] WANG Xiao-qing, CHOU K. Effects of thermal cycles on the microstructure evolution of Inconel 718 during selective laser melting process [J]. Additive Manufacturing, 2017, 18: 1−14.

[29] TANG Ling, LIANG Jing-jing, CUI Chuan-yong, LI Jin-guo, ZHOU Yi-zhou, SUN Xiao-feng, DING Yu-tian. Precipitation and phase transformation mechanism of

additive manufactured Ni−Co base superalloy [J]. Materials Characterization, 2019, 151: 252−259.
[30] XIAO H, LI S M, XIAO W J, LI Y Q, CHA L M, MAZUMDER J, SONG L J. Effects of laser modes on Nb segregation and Laves phase formation during laser additive manufacturing of nickel-based superalloy [J]. Materials Letters, 2017, 188: 260−262.
[31] XING H, DONG X L, CHEN C L, WANG J Y, DU L F, JIN K X. Phase-field simulation of tilted growth of dendritic arrays during directional solidification [J]. International Journal of Heat and Mass Transfer, 2015, 90: 911−921.
[32] RAGHAVAN N, DEHOFF R, PANNALA S, SIMUNOVIC S, KIRKA M, TURNER J, CARLSON N, BABU S S. Numerical modeling of heat-transfer and the influence of process parameters on tailoring the grain morphology of IN718 in electron beam additive manufacturing [J]. Acta Materialia, 2016, 112: 303−314.
[33] HAINES M, PLOTKOWSKI A, FREDERICK C L, SCHWALBACH E J, BABU S S. A sensitivity analysis of the columnar-to-equiaxed transition for Ni-based superalloys in electron beam additive manufacturing [J]. Computational Materials Science, 2018, 155: 340−349.
[34] ZHOU Y Z, VOLEK A, GREEN N R. Mechanism of competitive grain growth in directional solidification of a nickel-base superalloy [J]. Acta Materialia, 2008, 56(11): 2631−2637.

镍基高温合金 SLM 过程中熔池内的微观结构演变数值模拟

邱 义[1]，李应举[2]，冯小辉[2]，张 昂[3]，杨院生[2]

1. 北京理工大学 材料学院，北京 100081；
2. 中国科学院 金属研究所，沈阳 110016；
3. 重庆大学 材料科学与工程学院，重庆 400044

摘 要：采用有限元耦合相场的方法研究 IN718 高温合金在激光选区熔化过程中熔池内的竞争性生长和晶粒/枝晶结构的演变。通过有限元解决热演化问题，然后将结果输入相场模型，相场模拟涉及晶粒成核、晶粒外延生长和晶粒竞争的微观结构演变。基于对熔池横向和纵向截面微观结构演变的分析，讨论 SLM 过程中枝晶竞争性生长的机制，并量化计算熔池中溶质元素 Nb 的浓度分布。结果表明，枝晶竞争性生长受温度梯度和晶体学取向的影响，具有高错配角(>22.5°)的不利取向晶粒将很快被有利取向晶粒淘汰。

关键词：镍基高温合金；激光选区熔化；相场法；晶粒/枝晶结构演变；竞争生长

(Edited by Xiang-qun LI)